

Article

# Effect of Selected Cooling and Deformation Parameters on the Structure and Properties of AISI 4340 Steel

Maros Eckert <sup>1,\*</sup>, Michal Krbata <sup>1</sup>, Igor Barenyi <sup>1</sup>, Jozef Majerik <sup>1</sup>, Andrej Dubec <sup>2</sup> and Michal Bokes <sup>3</sup>

<sup>1</sup> Faculty of Special Technology, Alexander Dubcek University of Trenčín, 911 06 Trenčín, Slovakia; michal.krbata@tnuni.sk (M.K.); igor.barenyi@tnuni.sk (I.B.); jozef.majerik@tnuni.sk (J.M.)

<sup>2</sup> Faculty of Industrial Technologies, Alexander Dubcek University of Trenčín, 020 01 Puchov, Slovakia; andrej.dubec@tnuni.sk

<sup>3</sup> Faculty of Military Technology, University of Defence in Brno, 662 10 Brno, Czech Republic; michal.bokes@unob.cz

\* Correspondence: maros.eckert@tnuni.sk

Received: 3 November 2020; Accepted: 3 December 2020; Published: 7 December 2020



**Abstract:** The paper is focused on investigation of the high-strength AISI 4340 steel at various temperature and deformation conditions. The article is divided into two specific analyses. The first is to examine the dilatation behavior of the steel at eight different cooling rates, namely, 100, 10, 5, 1, 0.5, 0.1, 0.05 and  $0.01\text{ }^{\circ}\text{C}\cdot\text{s}^{-1}$ . The mapping of the phase transformations due to varying cooling rates from the austenitizing temperature of  $850\text{ }^{\circ}\text{C}$  allows the construction of the CCT diagram for a given high-strength steel. These dilatation curves were also compared with the metallography of the selected samples for the proper construction of the CCT diagram. A further analysis of the high temperature deformation of high strength steel AISI 4340 was performed in the range of temperature  $900\text{--}1200\text{ }^{\circ}\text{C}$ , and the strain rate was in the range from  $0.001$  to  $10\text{ s}^{-1}$  with maximum value of the true strain 0.9. Changes in the microstructure were observed using light optical microscopy (LOM). The effect of hot deformation temperature on true stress, peak stress and true strain was investigated. The hardness of all deformed samples, depending on the temperature, the deformation rate and the peak stress  $\sigma_p$  overall together related with hardness, has also been evaluated.

**Keywords:** dilatometry; CCT diagram; true stress; true strain

## 1. Introduction

Deformation and dilatometric analysis are nowadays a widespread method for evaluating changes in the microstructure in steels, and at the same time they are associated with changes in the resulting mechanical properties [1]. Phase changes are the main goal of these measurements in the case of dilatometric examination. The influence of the heating rate on the austenitic temperature and its subsequent holding time plays a very important role in the dilatometry process [2]. Most experiments focus more on lower carbon steels [3,4]. Low or medium alloy steels, which are classified as ferritic steels, are also investigated [5,6]. The investigated steel AISI 4340 is classified as a medium alloy steel, the main alloys are Ni, Cr, Mo, V. Due to its mechanical properties and high strength, the investigated steel belongs to special high-strength steels, which are used for manufacturing of military equipment. Steel is used mainly on tank barrels and other highly loaded parts in this technique due to good material fatigue resistance.

Experimental steel AISI 4340 shows the presence of several types of carbides in the material microstructure. These carbides are mainly based on Fe, Ni, Cr, Mo and V. The occurrence of

mainly these types of carbides  $M_2C$ ,  $M_7C_3$ ,  $M_{23}C_6$  and  $M_3C$  is mentioned [7,8]. These hard carbide particles contribute to grain refinement by retarding the recrystallization of austenite and causing the strengthening by this mechanism [9]. Alloying element presence also noticeably affects austenite transformation, mainly through the shift of start and finish temperatures of phase transformations [10].

The results obtained by the dilatometer are used to construct various types of diagrams that are closely related to the heat treatment of steels. One of these diagrams is the Continuous Cooling Transformation (CCT) diagram. These focus on the anisotropic decay of austenite and forming new structures. During the measurement, the expansion curve deviation from its linear direction during cooling or heating is monitored. Based on this deviation, it is possible to determine the initial temperatures  $Ac_1$  and  $Ac_3$ .

The CCT diagram gives information about the hardening response of steels and the nature of austenite transformation at varying degrees of cooling. This diagram has great practical importance to some heat treatment process such as austempering and isothermal annealing. The chemical composition of the investigated steels plays the most important role in the given process and influences the formation of the final microstructure. Likewise, the cooling rate of the sample is a very important factor in this process, examined by Lin et al. [11].

Phase transformations caused by temperature change can also be noticeably affected by application of proper deformation resulting to significant change of mechanical properties [12]. Application of the deformation brings effect at wide range of temperatures. If the deformation is applied at high temperatures with recrystallization effect, austenitic grain refinement occurs due to the repeated recrystallization what leads to improvement of mechanical properties. More noticeable effect to microstructure occurs at lower temperatures without recrystallization effect. The austenitic grains remain deformed and the deformation strips are formed inside them. Consequently, new phase (martensite) nucleates not only as a standard at grain boundaries but also inside the grain at the deformation strips. Nucleation within the deformed austenitic grains is one of the most important aspects of thermo-mechanical processing [13–15].

The material acts against every deformation, and this reaction is called deformation resistance. The deformation resistance is related to the temperature, deformation rate and the value of the deformation. Therefore, stress affecting the material must be higher than deformation resistance in order to achieve plastic deformation and consequently required shape change of the material. The forging of semi-products at higher temperatures is also one of the fundamental steps in the production of advanced high-strength steel. The combination of phase transformation and the forging (deformation) allow significant increase of the steel strength properties. The investigations using quenching and deformation dilatometer were carried out with controlling different deformation parameters, i.e., the degree of deformation (by how much the sample is to be deformed), the deformation rate and the temperature at which the deformation occurs [16,17].

The first goal of this paper is to investigate phase transformations of AISI 4340 high strength steel depending on the different cooling conditions. Subsequently, the creation of a CCT diagram for a given steel based on the achieved experimental data. The second goal is to investigate the deformation behavior of the steel at high temperatures and then to create corresponding True Stress–True Strain diagrams and investigate the relation between deformation parameters and deformation resistance. The contribution of the work is a complex evaluation of the investigated material AISI4340 from the point of view of thermo-mechanical processing and determination of the influence of selected parameters on the change of the experimental material structure in the monitored processes. It is also beneficial to create a corrected constitutive model in terms of friction during compression.

## 2. Materials and Methods

### 2.1. Experimental Material

The experimental steel that was used for the measurements is referred to as AISI 4340. Steel (Konstrukta Defence; Trenčín, Slovakia) is used for components in special technology, withstands high fatigue loads and is characterized by high strength while maintaining sufficient toughness.

The chemical composition of the delivered steel was verified (Table 1). This analysis was performed on a special Q4 TASMAN chemical analyzer. Verification of the chemical composition was compared with the ISO 4967 standard. Table 2 also shows the basic mechanical properties of the examined steel [18].

**Table 1.** Chemical composition of the AISI 4340 examined steel (wt.%).

Element	C	Mn	Si	Cr	Ni	Mo	V
Min	0.33	0.25	0.17	1.20	1.65	0.35	0.10
Max	0.40	0.50	0.37	1.50	2.00	0.45	0.80
Spectral analysis	0.40	0.30	0.32	1.49	1.98	0.52	0.13

**Table 2.** Basic properties of the AISI 4340 steel.

Tensile Strength $R_m$ (MPa)	Modulus of Elasticity $E$ (GPa)	Thermal Conductivity (W·m <sup>-1</sup> ·K <sup>-1</sup> )	Hardness (HV5)	Specific Heat (J·kg <sup>-1</sup> ·K <sup>-1</sup> )
1500	210	20	596	460

Microstructure of investigated AISI 4340 steel (Figure 1a) was analyzed with using of light microscope Neophot 32 (ZEISS, Oberkochen, Germany) as well as SEM microscope Tescan Vega (Tescan, Brno, Czech Republic) (Figure 1b). The samples were etched by Nital (3% solution of nitric acid in ethanol). The microstructure of the supplied material is made of tempered martensite, bainite and fine secondary carbides, which are spherical in shape. The final structure is coarse-grained and relatively heterogeneous. The microstructure evaluated corresponds to the state after quenching and tempering of thick-walled Cr-Ni-Mo-V steels.

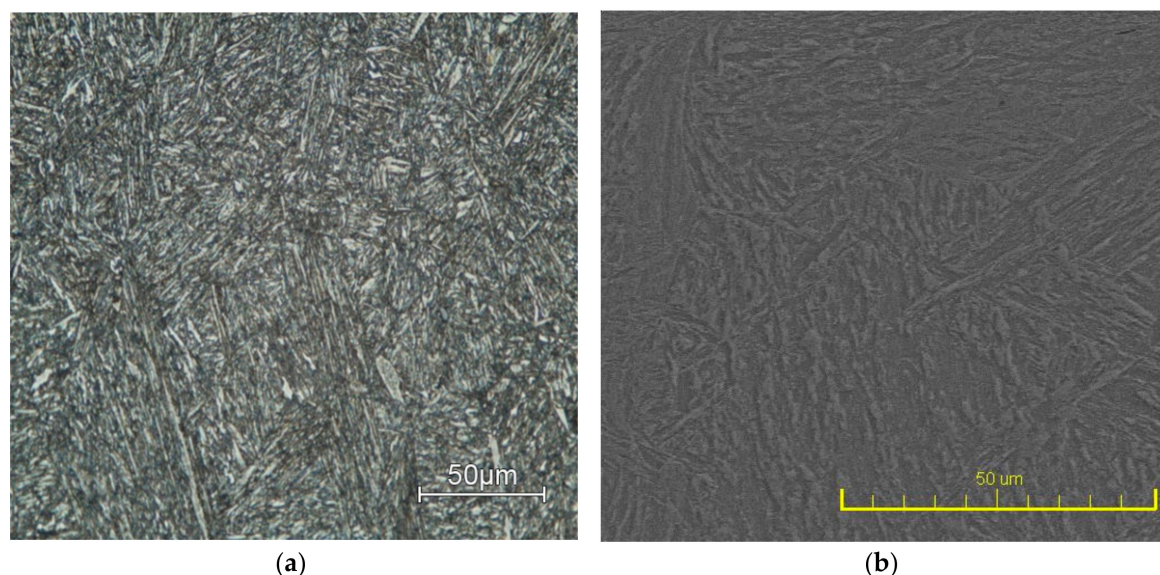


**Figure 1.** Microstructure of base material AISI 4340, etching by 3% Nital: (a) LOM; (b) SEM.

Two different martensite morphologies occurred in steel in the delivered state. The first form was represented by lath martensite, and the second was the occurrence of plate martensite. Lattice martensite occurs predominantly in steels that have a lower carbon content and medium content of additive alloying elements. In contrast to steels with a medium carbon content, martensite morphology is formed with both types. Small dimension of the lath martensite structure brings significant effect on the strengthening mechanism.

## 2.2. Continuos Cooling Transformation

The process in which homogeneous austenite decays into other structures during continuous cooling is called anisothermal decay of austenite. The resulting CCT diagrams express a graphical representation of this process. The cooling rate, which affects the formation of the final structure, has an analogous effect on the resulting decomposition of austenite [19,20].

All dilatometers utilize measurement of dimensions (length and/or diameter) and temperatures during heating and cooling. Each material consists of millions of atoms that are interconnected, and due to the increase in temperature, these atoms begin to move (oscillate). The total volume of material begins to change, which is associated with a change in the length of the material. The thermal expansion of all crystalline substances is directly related to the action of internal atomic forces in the crystal lattice [21].

Depending on the temperature, the resulting phase change reflects itself in a linear dilatation curve as a deviation of the direction of this curve, and its length changes on the experimental material. The temperature  $Ac_1$  examines the start of austenite formation when the material is heated due to the deviation of the dilatation curve from its linear direction. The final transformation of austenite formation occurs at the temperature  $Ac_3$ , where again the dilatation heating curve begins to have its linear character.

Phase transformation studies were carried out using DIL805A/D dilatometer (TA Instruments, Milford, MA, USA), and the critical transformation points (temperatures) were determined according to [22–24]. The heating rate was  $1\text{ }^{\circ}\text{C}\cdot\text{s}^{-1}$  with holding time 30 min. at an austenitizing temperature of  $850\text{ }^{\circ}\text{C}$ . The cooling rate ranged from  $100\text{ }^{\circ}\text{C}\cdot\text{s}^{-1}$  to  $0.01\text{ }^{\circ}\text{C}\cdot\text{s}^{-1}$ . Cooling regimens used for construction the CCT diagram of AISI 4340 steel are shown in Figure 2.

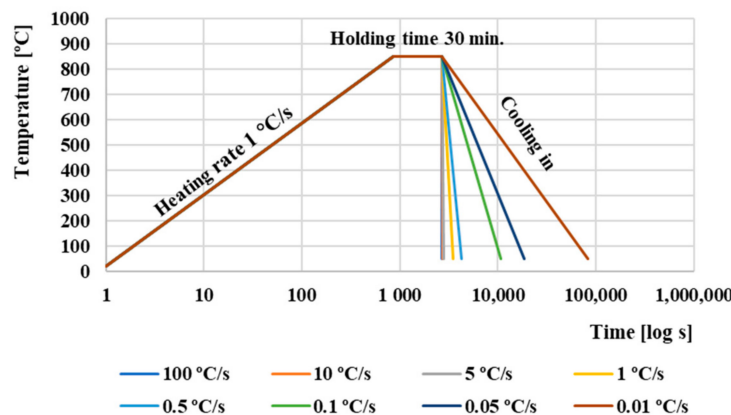


**Figure 2.** Heating and cooling regimens used for construction the CCT diagram of AISI 4340 steel.

Samples were made in form of cylinder with diameter of 4 mm and length of 10 mm. Each experiment was repeated 4 times, and averages were calculated to obtain relevant values. The CCT diagram also shows the resulting hardness values, which were measured using Instron Wolpert (Instron, Norwood, MA, USA) hardness tester. Vickers method HV5 was used with load 50 N. Hardness was measured 5 times on each sample.

### 2.3. Investigation of Rheology

Deformation dilatometer (TA Instruments, Milford, MA, USA) used in this study utilizes compression of the samples in axisymmetric test. The results of the experiments are presented in form of true stress–true strain curves, Figure 3. It is a relation between the true stress and corresponding true strain, also called flow stress curves. Elastic deformation has a negligible value and therefore is omitted. There are four characteristic points in the curve. The point  $[0; \sigma_0]$  is onset of plastic deformation. Stress  $\sigma_0$  could be considered as yield point in a compression. The point  $[\varphi_p; \sigma_p]$  is the maximal value of stress, marked as  $\sigma_p$ . Several authors describe the value as a Peak Stress [25,26].

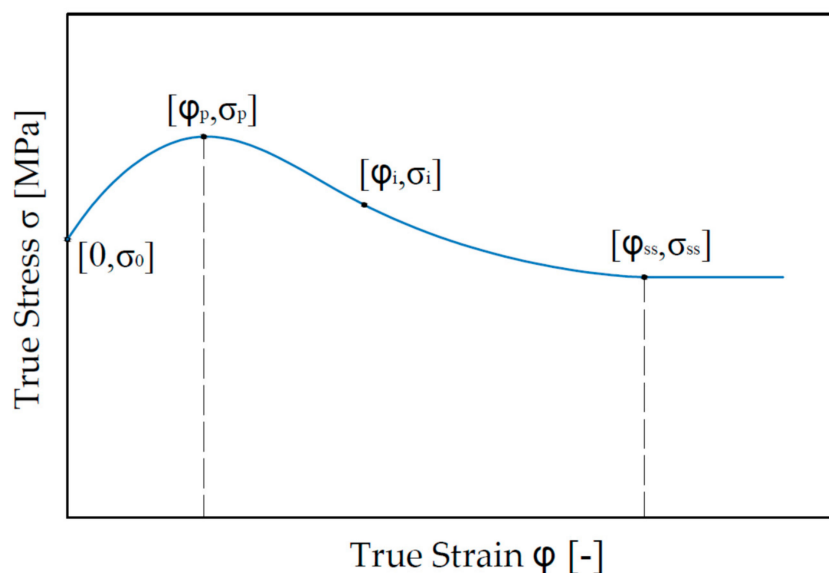


**Figure 3.** Typical True stress–True strain dependence of steels.

Consequently, the strain value corresponding with the peak stress is described as peak strain. The coordinates  $[\varphi_i; \sigma_i]$  define the inflectional point of the curve. The point  $[\varphi_{ss}; \sigma_{ss}]$  is an equilibrium point from which strengthening and softening mechanisms are in balance. Therefore, the meaning of lower index “ss” is steady state.

Defined input parameters for compression test using of DIL 805A/D are temperature ( $t$ ), deformation ( $\varphi$ ) and deformation rate ( $\dot{\varphi}$ ). The experiments were performed at temperatures of 900, 1000, 1100 and 1200 °C; strain rate from 0.001 to 10 s<sup>-1</sup> and maximum strain 0.9. At the end of experiment, all samples were cooled at a constant cooling rate 20 °C/s. Samples were made in form of cylinder with diameter of 5 mm and length of 10 mm. Moreover, in these experiments, average values were obtained from 4 identical measurements to obtain relevant values. Due to the friction of the contact surfaces between the sample and the compression pistons of the dilatometry device, the stresses were corrected as [27]:

$$\sigma = \frac{\sigma_0 C^2}{2[\exp(C) - C - 1]} \quad (1)$$

where  $\sigma$  is the friction corrected true stress, and  $\sigma_0$  is the measured true stress. Parameter  $C$  can be determined as:

$$C = \frac{2mR}{h} \quad (2)$$

$R$  and  $h$  are instantaneous radius and height of specimen, and  $m$  is the friction coefficient. Geometrical parameters can be determined according to the amount of barreling for specimen and the friction coefficient then is calculated as

$$m = \frac{\left(\frac{R}{h}\right)b}{\left(\frac{4}{\sqrt{3}}\right) - \left(\frac{2b}{3\sqrt{3}}\right)} \quad (3)$$

where  $R$  is the theoretical radius,  $h$  is the final height of the sample after compression, and  $b$  is the barreling factor. The theoretical radius  $R$  can be determined as

$$R = R_0 \sqrt{\frac{h_0}{h}} \quad (4)$$

and barreling factor as

$$b = 4 \frac{\Delta R}{R} \cdot \frac{h}{\Delta h} \quad (5)$$

where  $R_0$  and  $h_0$  are the initial dimension of sample,  $\Delta h$  is the difference between the initial and final height of the sample, and  $\Delta R$  is the difference between the largest and smallest radii of the deformed sample.

The values of the geometric parameters of the sample before compression were  $R_0 = 5$  mm and  $h_0 = 10$  mm. After compression, the average values of the geometric parameters were  $\Delta R = 0.81$  mm and  $\Delta h = 5.93$  mm. Based on these parameters,  $m = 0.358$  and  $C = 0.564$  were determined. Using these parameters and Equation (1), the values of the measured true stresses were corrected.

#### 2.4. Constitutive Model

For this material, we chose a mathematical model based on the Arrhenius equation. This model is represented by the equation [28]

$$Z = \dot{\varphi} \exp\left(\frac{Q}{RT}\right) \quad (6)$$

and

$$\dot{\varphi} = AF(\sigma) \exp\left(-\frac{Q}{RT}\right) \quad (7)$$

where  $\dot{\varphi}$  is strain rate,  $A$  is material constant,  $Z$  is Zener–Hollomon parameter,  $R$  is the gas constant (8.314 J/mol·K),  $Q$  is the activation energy and acts as an indicator of deformation difficulty in the physical deformation theory, and  $T$  is the temperature [29]. The  $Z$  parameter represents the temperature compensated strain rate, which has been widely used to characterize the behavior of materials in hot working [30].  $F(\sigma)$  is a function of flow stress and can be described as follows:

$$F(\sigma) = \begin{cases} \sigma^n & \alpha\sigma < 0.8 \\ \exp(\beta\sigma) & \alpha\sigma > 1.2 \\ [\sinh(\alpha\sigma)]^n & \text{for all } \sigma \end{cases} \quad (8)$$

where  $n$ ,  $\beta$ , and  $\alpha$  are material constants and can be determined from experimental flow stress data. The material constant  $\alpha$  is determined using the parameters  $n'$  and  $\beta$  defined as [31]

$$n' = \left[ \frac{\partial \ln \dot{\varphi}}{\partial \ln \sigma} \right]_T \quad (9)$$

and

$$\beta = \left[ \frac{\partial \ln \dot{\varphi}}{\partial \sigma} \right]_T \quad (10)$$

Consequently, the parameter  $\alpha$  is

$$\alpha = \frac{\beta}{n'} \quad (11)$$

By combining Equations (7) and (8) for all stress levels (low and high), the strain rate can be expressed as

$$\dot{\varphi} = A[\sinh(\alpha\sigma)]^n \exp\left(-\frac{Q}{RT}\right) \quad (12)$$

and its logarithm as

$$\ln[\sinh(\alpha\sigma)] = \frac{\ln \dot{\varphi}}{n} + \frac{Q}{nRT} - \frac{\ln A}{n} \quad (13)$$

By differentiating Equation (13) at constant temperature,

$$\frac{1}{n} = \left[ \frac{\partial \ln[\sinh(\alpha\sigma)]}{\partial \ln(\dot{\varphi})} \right] \quad (14)$$

where the parameter  $n$  can again be determined as the reciprocal value of the average slopes of the linear fitting between  $\ln[\sinh(\alpha\sigma)]$  and  $\ln(\dot{\varphi})$ . Moreover, from this dependence, parameter  $A$  is determined from the intercept of the linear fitting according to

$$\ln A = \frac{Q}{RT} + \frac{C}{n} \quad (15)$$

where  $C'$  represents the intercept of the linear fitting for each temperature. From Equation (12) it is possible to determine for each strain rate the dependence between  $\ln[\sinh(\alpha\sigma)]$  and  $1000/T$ . Average value of the linear fitting slopes from this plot expresses the  $Q/Rn$ , and thus, the hot deformation activation energy  $Q$ . Then the flow stress based on the mathematical model will be

$$\sigma = \frac{1}{\alpha} \ln \left\{ \left( \frac{Z}{A} \right)^{\frac{1}{n}} + \left[ \left( \frac{Z}{A} \right)^{\frac{2}{n}} + 1 \right]^{\frac{1}{2}} \right\} \quad (16)$$

### 3. Results and Discussion

The first results we focused on in our research were aimed at finding two initial temperatures:  $Ac_1$  and  $Ac_3$ . The heating of all eight samples took place under the same conditions, i.e., the heating rate was set to  $1 \text{ } ^\circ\text{C}\cdot\text{s}^{-1}$ . Figure 4a explains how we initially determined the temperatures of  $Ac_1$  and  $Ac_3$ . The results showed that in the experimental steel AISI 4340, the start temperature of  $Ac_1$  was  $725 \text{ } ^\circ\text{C}$ , and the final temperature of austenite formation  $Ac_3$  was  $763 \text{ } ^\circ\text{C}$ .

The start and finish of the austenitization temperatures are shown to a greater extent in Figure 4b. The linear dilatation curves are crossed by tangent lines, which help us to accurately determine the initial temperatures when heating  $Ac_1$  and  $Ac_3$ . Another helpful function is the derivation of the dilatation curve on which we can also observe the deviation of the dilatation curve from its linear direction. Using derivation of dilatation curves, we can more accurately determine the exact point of deviation of the curve.

After determining the initial temperatures,  $Ac_1$  and  $Ac_3$ , on heating the samples, we focused on the following dilatation curves, which represented different cooling rates. These following eight dilatation curves investigate the decomposition of austenite at different cooling rates and the formation of the resulting microstructure. The formation of the final phases after cooling does not only have to be homogeneous but can be formed by a combination of several structures. The rate of cooling affects the formation of the final microstructure. Each resulting phase transformation has its own temperature ranges at which it can occur. These thermal ranges can represent a relatively wide range of formation of the follow structure, which occurs in the process of anisothermal decomposition of austenite.

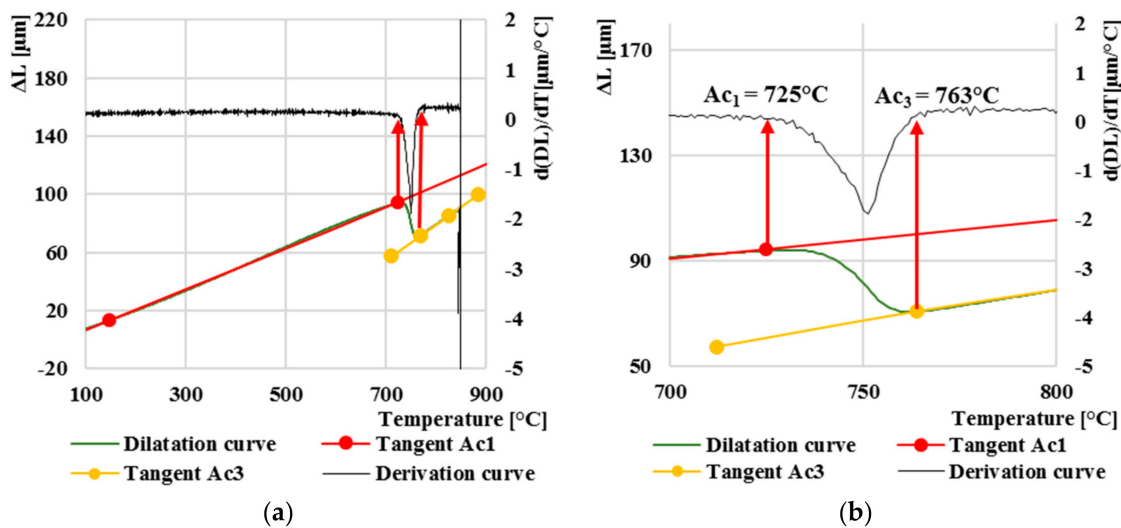


**Figure 4.** (a) Dilatation curve on heating; (b) Enlarged part (zooming) of the length change vs. temperature curve—determination of  $Ac_1$  and  $Ac_3$  temperatures.

From all eight curves, three dilatation curves for comparison were selected, which represent the limit values of the formation of individual phase transformations. At the highest cooling rate, i.e.,  $100\text{ }^\circ\text{C/s}$ , determined martensite start temperature  $Ms$  was  $321\text{ }^\circ\text{C}$ . Figure 5a shows a green line of the dilatation curve, which is covered by a red tangent line. For a more accurate determination, the figure is supplemented by the superimposed derivation of the given dilatation curve (Figure 5a, black line). At this high cooling rate, the resulting structure was evaluated as martensitic with a small percentage of retained austenite, which was not further investigated in this paper.

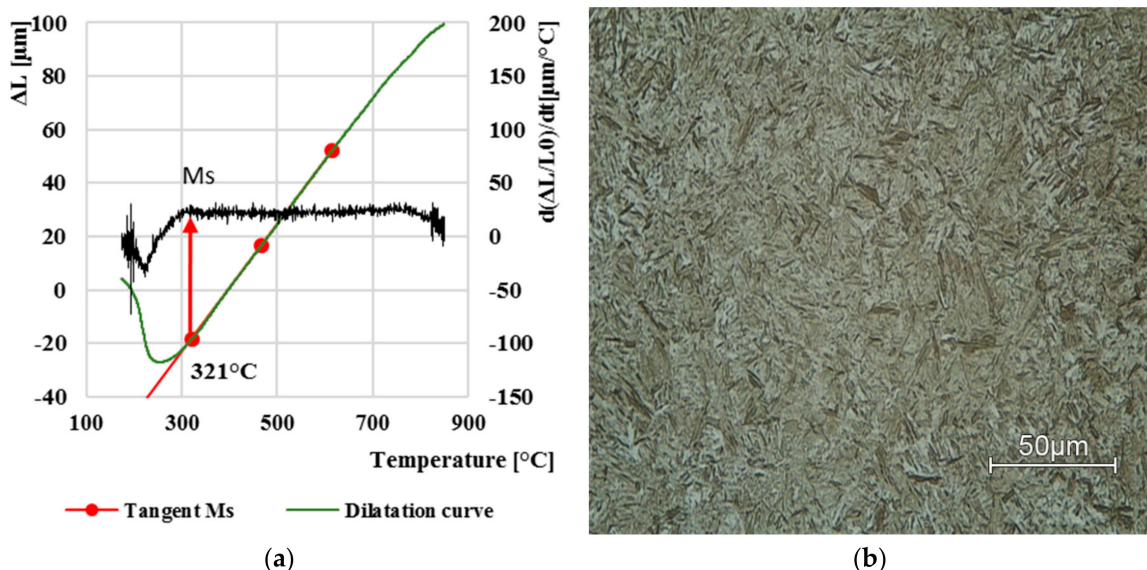


**Figure 5.** Dilatation curve (a); the final microstructure LOM (b) after cooling at  $100\text{ }^\circ\text{C}\cdot\text{s}^{-1}$ .

Another evaluated curve was at a cooling rate of  $0.5\text{ }^\circ\text{C}\cdot\text{s}^{-1}$ . We can observe that the initial temperature of martensite formation had a lower value, namely  $292\text{ }^\circ\text{C}$  (Figure 6a). With enough increase in the dilatation curve, a small dilatation change was also observed at  $480\text{ }^\circ\text{C}$ , which represents the beginning of the bainite transformation. According to the dilatation curve, the resulting microstructure is again martensitic with a very low bainite content (Figure 6b).

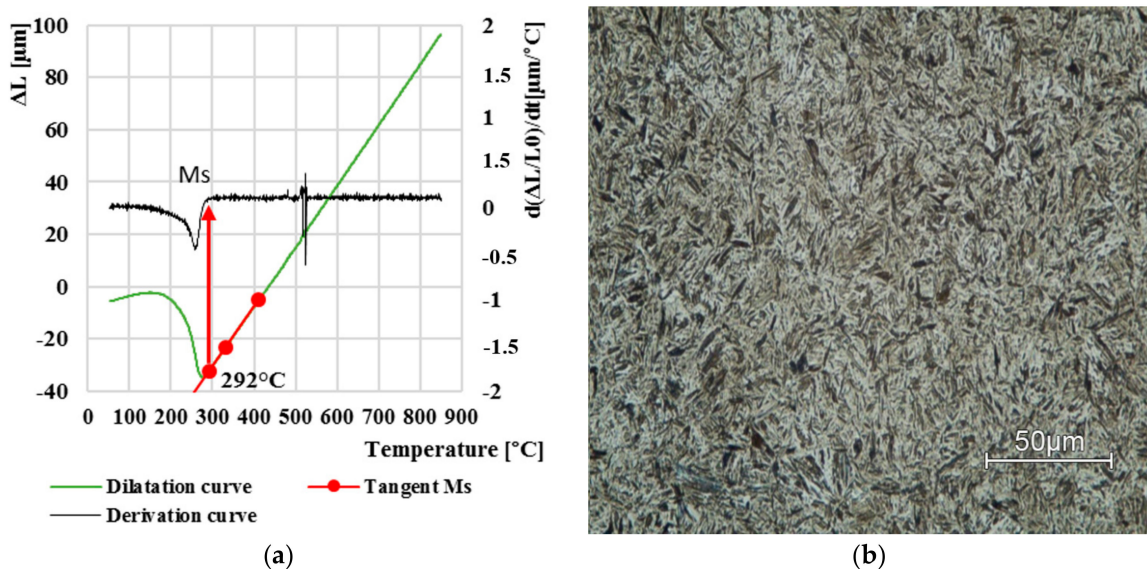


**Figure 6.** Dilatation curve (a); the final microstructure LOM (b) after cooling at  $0.5\text{ }^{\circ}\text{C}\cdot\text{s}^{-1}$ .

Lastly, we examined the dilatation curve at cooling of  $0.01\text{ }^{\circ}\text{C}\cdot\text{s}^{-1}$ , which can be observed in Figure 7a. Up to three phase transformations occurred in this resulting structure, namely, ferritic, bainitic and martensitic. The ferritic began at  $700\text{ }^{\circ}\text{C}$ . Subsequently, a bainitic transformation began at temperature of  $476\text{ }^{\circ}\text{C}$ . The start of the martensitic transition did not occur until  $158\text{ }^{\circ}\text{C}$ . Final microstructure comprised bainite matrix with polygonal ferrite and a very small amount of martensite (Figure 7b).

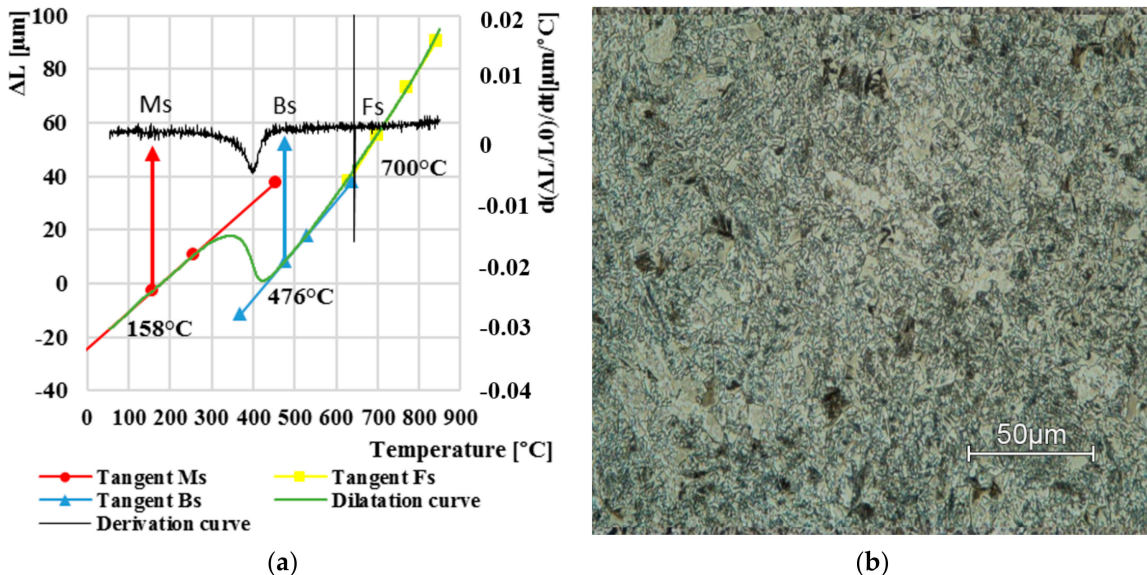


**Figure 7.** Dilatation curve (a); the final microstructure LOM (b) after cooling at  $0.01\text{ }^{\circ}\text{C}\cdot\text{s}^{-1}$ .

The average temperature of  $Ms$  was determined from the dilatation curves in which only the martensite structure was formed. We used the first five cooling curves from  $100\text{ }^{\circ}\text{C}\cdot\text{s}^{-1}$  to  $0.5\text{ }^{\circ}\text{C}\cdot\text{s}^{-1}$ . The results are shown in Figure 8. By averaging these five temperatures from the individual curves, the average temperature  $Ms$  was of  $282\text{ }^{\circ}\text{C}$ . We could not measure the temperature  $Mf$  on any curve, because the austenite to martensite transformation occurred below RT (room temperature). We can observe that as the cooling rate lowers, the temperature  $Ms$  also decreases.

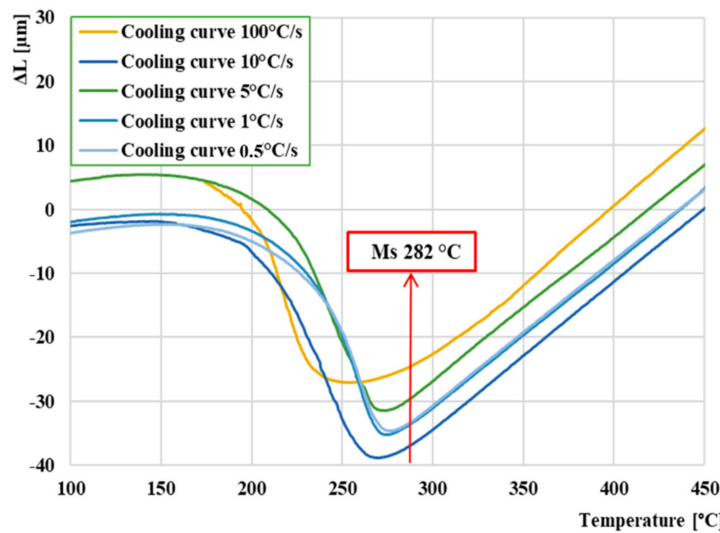


**Figure 8.** Comparison and determination of average temperature  $M_s$ .

### 3.1. CCT Diagram AISI 4340 Steel

The construction of the CCT diagram (Figure 9) of the experimental steel AISI 4340 was created from all eight expansion curves. For its accurate compilation, it was necessary to analyze dilatation curves and evaluate the microstructure of the measured samples, which confirms the formation of the phases in the dilatation curves. The austenitization temperature was set at  $850\text{ }^{\circ}\text{C}$ , and the heating rate of all samples was  $1\text{ }^{\circ}\text{C}\cdot\text{s}^{-1}$ . To achieve the transformation of the austenite in the whole sample volume, the holding time at the austenitizing temperature was 30 min. We determined the temperatures of  $A_{c1}$  and  $A_{c3}$  using expansion curves during heating. The CCT diagram of experimental high-strength steel AISI 4340 consists of three transformation phases. The first phase occurred in the first four dilatation curves up to a cooling rate of  $1\text{ }^{\circ}\text{C}\cdot\text{s}^{-1}$  and consists only in martensite. We observed the formation of a second phase at a cooling rate of  $0.5\text{ }^{\circ}\text{C}\cdot\text{s}^{-1}$ , which was a bainite. This resulting bainitic region continues until the last dilatation curve, which has been cooled at a rate of  $0.01\text{ }^{\circ}\text{C}\cdot\text{s}^{-1}$ .

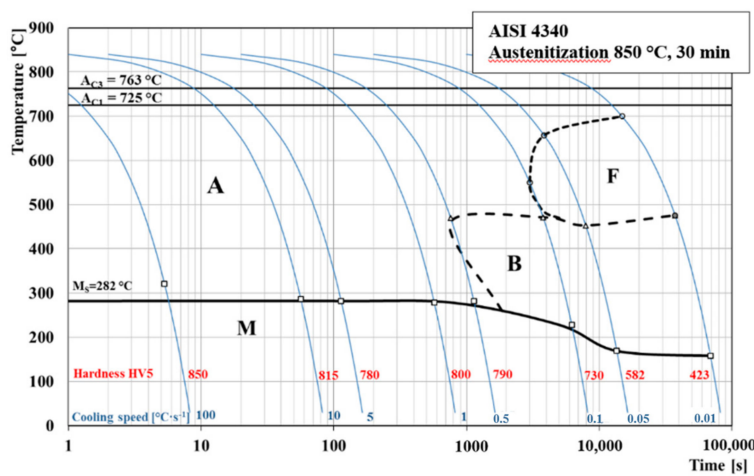


**Figure 9.** CCT diagram of AISI 4340 steel.

A third transformation phase also occurred in the CCT diagram, which is located above the bainitic region and is formed by a ferrite. The ferritic transformation region occurred only at the last three cooling curves, namely  $0.1, 0.05$  and  $0.01\text{ }^{\circ}\text{C}\cdot\text{s}^{-1}$  [32,33].

The end of all measurements was set at  $50\text{ }^{\circ}\text{C}$ . For this reason, in the CCT diagram, there is no boundary region of martensite formation  $M_f$ . This is because it lies in negative temperatures, and our

device does not currently allow negative temperatures to be set. As already mentioned, the resulting  $M_s$  temperature was evaluated from the first dilatation curves and has a value of 282 °C. According to the CCT diagram, this temperature represents the limit value at which a martensite begins to form in the structure of the material. In order to avoid the formation of a possible heterogeneous structure, the specific cooling rate must be maintained.

We can also observe in the diagram that the hardness declined due to the decreasing cooling rate. This result is associated with the formation of the microstructure after cooling the samples. The highest Vickers hardness 850 was reached at the highest cooling rate of 100 °C·s<sup>-1</sup>. The hardness results differed only slightly, where the microstructure was formed only by martensite. We observe that the hardness began to decrease after the beginning of the formation of a heterogeneous structure (bainite + martensite). Significant decrease in hardness occurred during the formation of ferrite. Final Vickers hardness of 423 was measured in the last dilatation curve, which was cooled at a rate of 0.01 °C·s<sup>-1</sup>. This represents an almost 50% decrease compared to the highest cooling rate of 100 °C·s<sup>-1</sup>. The arrangement of the ferrite atomic lattice is of the bcc type, while the martensitic structure creates a bct atomic lattice, which by its structure supports the increase of the material hardness [34–37].

Several authors have discussed the issue of creating a CCT diagram of a given steel. As is known, the main parameters that affect the overall shape of the CCT diagram are primarily the chemical composition. However, the set austenitization temperature is also an important factor. Boyer et al. [38] examined AISI 4340 steel from the point of view of creating its CCT diagram. The critical cooling rate at which only the martensite microstructure is formed was determined to be 8.3 °C·s<sup>-1</sup>. Our critical rate of pure martensitic transformation is 0.5 °C. Overall, their diagram is shifted to the left. Likewise, a group of authors, Samadi Shahreza et al. [39] and Penha et al. [40], dealt with this issue, and their resulting CCT diagrams are also slightly shifted to the left. Nasar A. Ali [41] and Popescu et al. [42] investigate a very similar steel with a slightly higher content of Cr and Ni. Their CCT diagrams match our measured diagrams in the critical transformation of martensite as well as in the overall shape of the diagram. Our CCT diagram does not include the beginning of pearlitic transformation because this transformation takes place only at very low cooling rates. The higher content of Cr and Ni in the investigated steel shifts the whole area of pearlitic transformation to the right. When comparing our diagram, the value of the temperature  $M_s$  coincides with other authors. Our material contains the upper limits of the main alloying elements, and this higher percentage of alloying elements, especially Cr and Ni, significantly affects the resulting shape and orientation of our CCT diagram when compared to other authors.

### 3.2. True Stress–True Strain Diagrams of AISI 4340 Steels

Basic input parameters for high temperature True Stress–True Strain curves are temperature, deformation rate and deformation degree. Deformation degree was set as constant ( $\Delta L = 0.6$ ), while other two parameters were variable during the experiment. There are used temperatures 900, 1000, 1100 and 1200 °C and deformation rates 10, 1, 0.1, 0.01, 0.001 s<sup>-1</sup> in the experiment. As a result, twenty True Strain–True Stress high temperature curves were measured. The measured flow stress data was corrected by Equation (1) due to the friction.

To create a constitutive model based on Arrhenius equation, it was necessary to determine the individual material constants. These constants are determined for each true strain value, in our case from  $\phi = 0.1$  to  $\phi = 0.8$  with a step of 0.05. The following will show the procedure for determining the parameters for true strain  $\phi = 0.2$ . The parameter  $n'$  is obtained as the reciprocal value of the slope between  $\ln(\sigma)$  and  $\ln(\dot{\phi})$  (Figure 10a). The parameter  $\beta$  is again determined as reciprocal value of the slope between  $\sigma$  and  $\ln(\dot{\phi})$  (Figure 10b). The average values of the slope determine the values of the parameters, namely  $n' = 5.603$  and  $\beta = 0.0787$ . Then, according to Equation (11),  $\alpha = 0.0141$ .

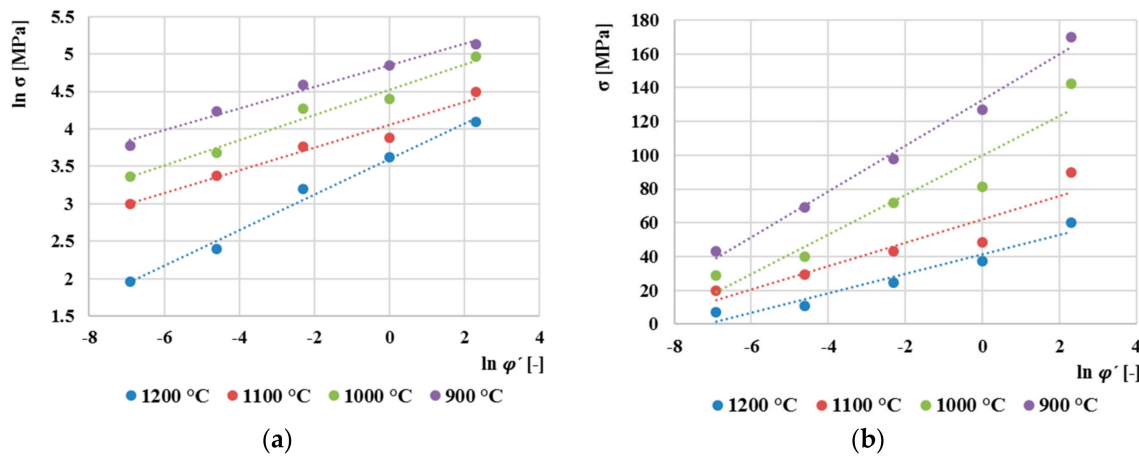


**Figure 10.** (a) Dependence between  $\ln \dot{\varphi}$  and  $\ln \sigma$  for derivation of  $n'$  parameter, (b) dependence between  $\ln \dot{\varphi}$  and  $\sigma$  for derivation of  $\beta$  parameter.

Based on Equation (14), a dependence was created (Figure 11a), from which the parameter  $n$  was determined as the average of the reciprocal values of linear fittings ( $n = 3.564$ ). The activation energy value  $Q$  is determined based on the graphical dependence shown in Figure 11b. The average value of the activation energy for the material AISI 4340 was calculated  $Q = 314$  kJ/mol. This value is lower compared to [43], where the value  $Q = 427$  kJ/mol was obtained, where the values of flow stresses were not corrected by the effect of friction during compression. On the contrary, a lower value of activation energy,  $Q = 281.28$  kJ/mol, was obtained by the authors [44], where, however, this value was determined by expression for determining the activation energy as a function of chemical composition developed by [45]. This calculation was created for general use for low-alloy steels and therefore does not provide as accurate results as the values of the activation energy obtained from the measured flow stresses.

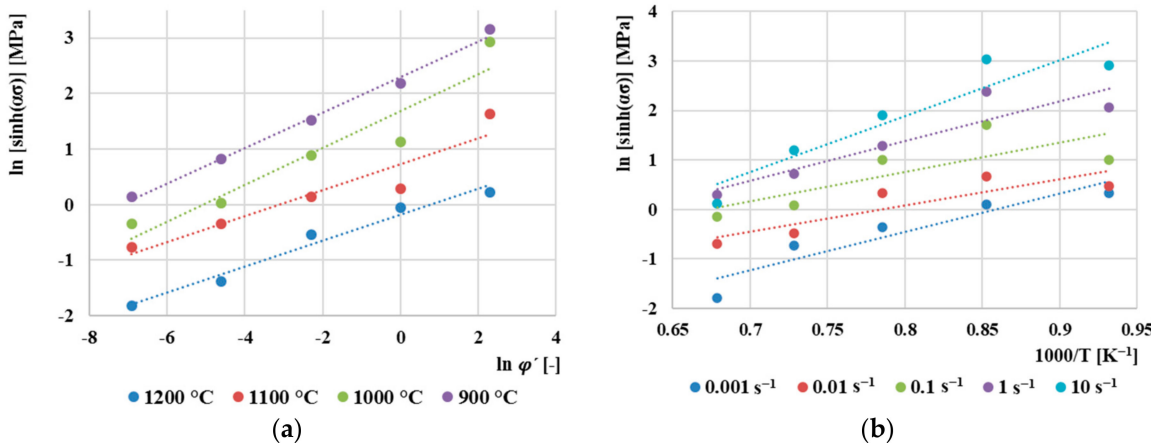


**Figure 11.** (a) Dependence between  $\ln[\sinh(\alpha\sigma)]$  and  $\ln(\dot{\varphi})$  for derivation of  $n$  parameter, (b) dependence between  $\ln[\sinh(\alpha\sigma)]$  and  $1000/T$  for derivation  $Q$  parameter.

The Zener–Hollomon parameter  $Z$  is determined according to Equation (6) for the respective true strain and the predicted flow stresses are calculated according to Equation (16) for all strain rate and deformation temperatures.

A comparison between the measured (lines) and experimentally obtained flow stresses (dots) is shown in Figure 12. The values and courses of stresses are highly dependent on the deformation temperature. A comparison of the curves shows that increasing strain rate or decreasing temperature causes an increase in flow stress. In other words, softening due to dynamic recrystallization and dynamic recovery is prevented and causes the material to exhibit strain hardening. The higher strain rate and lower temperature provide a shorter time for energy accumulation and lower mobility at the grain boundaries, which also leads to the growth of dynamically recrystallized grains and the partial removal of dislocations.

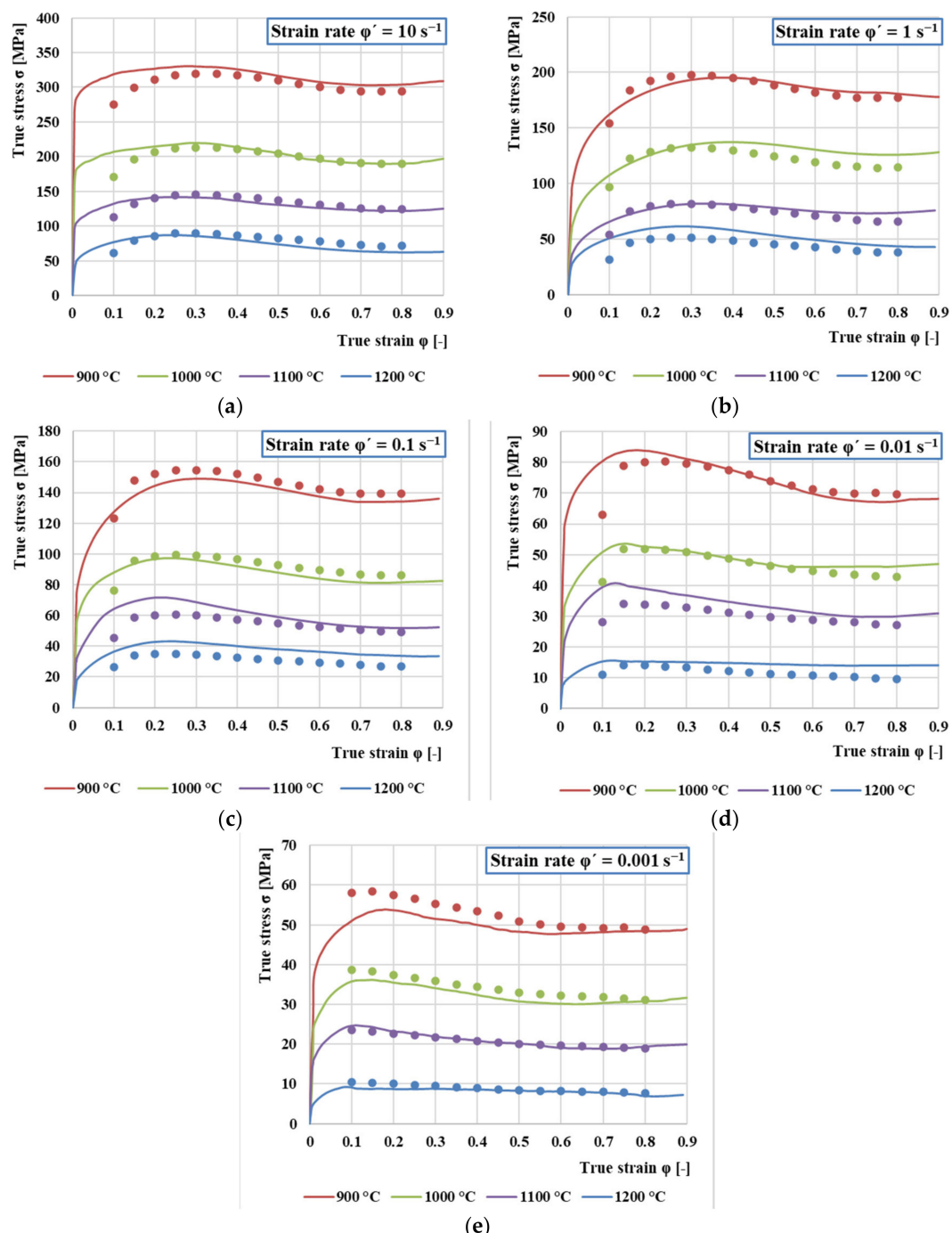


**Figure 12.** True Stress–True Strain Diagrams with measured (lines) and predicted (dots) flow stresses for (a) strain rate  $\dot{\varphi}' = 10 \text{ s}^{-1}$ ; (b) strain rate  $\dot{\varphi}' = 1 \text{ s}^{-1}$ ; (c)  $\dot{\varphi}' = 0.1 \text{ s}^{-1}$ ; (d)  $\dot{\varphi}' = 0.01 \text{ s}^{-1}$ ; (e)  $\dot{\varphi}' = 0.001 \text{ s}^{-1}$ .

For each curve, after a rapid increase of stress to the highest (peak) value, it begins to gradually decrease towards a steady state with varying degrees of softening, indicating the onset of dynamic recrystallization (DRX). Furthermore, all flow stress curves can be divided into three stages. In the first stage, in which there is a sharp increase in stress up to a critical value, the work hardening dominates. In the second stage, the increase in stress is constantly slowed down to the peak value or the inflection value of the work hardening rate, which corresponds to the increasing influence of dynamic recovery and recrystallization. This effect increases and at some point exceeds the effect of work hardening. The highest peak stress was measured at the strain rate  $\dot{\varphi}' = 10 \text{ s}^{-1}$  (328 MPa) and the lowest at the rate  $\dot{\varphi}' = 0.001 \text{ s}^{-1}$  (65 MPa). This means that at the highest rate, the peak stress reached five times bigger value. In the last third stage, two predominant curves can be observed. One is a continuous decrease with a significant DRX mechanism, which occurs especially at the lowest temperature ( $900^\circ\text{C}$ ) or higher transformation rates ( $1 \text{ s}^{-1}$ – $10 \text{ s}^{-1}$ ) in the entire range of deformation temperatures. The second is only a slight flow stress drop due to DRX. This course is especially visible at higher temperatures ( $1200$ – $1100^\circ\text{C}$ ). This is mainly because under these conditions, the higher speed of the DRX slows down the work hardening. This also shifts the peak and steady stresses to lower values of the true strain.

As can be seen from Figure 12, the predicted stress values using the Arrhenius-type constitutive model are in very good agreement with the measured values over the entire temperature range and strain rates. The Pearson's correlation coefficient  $R$  was calculated to determine the quality of the correlation between the measured and predicted values of flow stresses. The evaluation of the suitability of using the selected model for flow stress prediction of AISI 4340 steel is shown in Figure 13. The value of the coefficient of determination in comparison with the best fitting is  $R^2 = 0.9892$ .

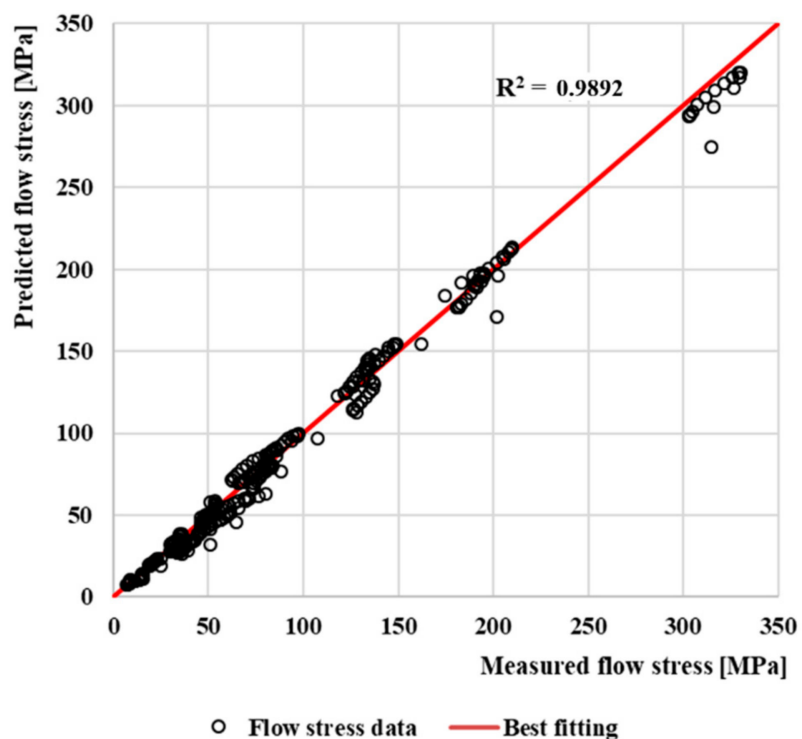


**Figure 13.** The correlation between predicted and measured flow stresses and comparation with best fitting.

Overall dependence of peak stress on temperature for individual strain rates is shown in Figure 14a. The peak stress values were obtained as the highest values of flow stresses from the dependences in Figure 12. The peak stress decreases linearly in relation to the deformation temperature. Similar results were obtained also by the authors [45]. Results clearly shows that the increasing temperature significantly affects deformation resistance of the material. When the material is heated to high temperatures in stable austenite area close to melting point, the interatomic distance increases. Distance between atoms in the crystal lattice increases, and consequently, strength of the material is reduced. Therefore, less force is required to deform the material. Figure 14b indicates the relationship between the peak stress and the logarithmic strain rate. The peak stress increases linearly in relation to the deformation rate. As with dependence on temperature in previous chapter, results clearly shows that the increasing deformation rate significantly affects deformation resistance of the material.

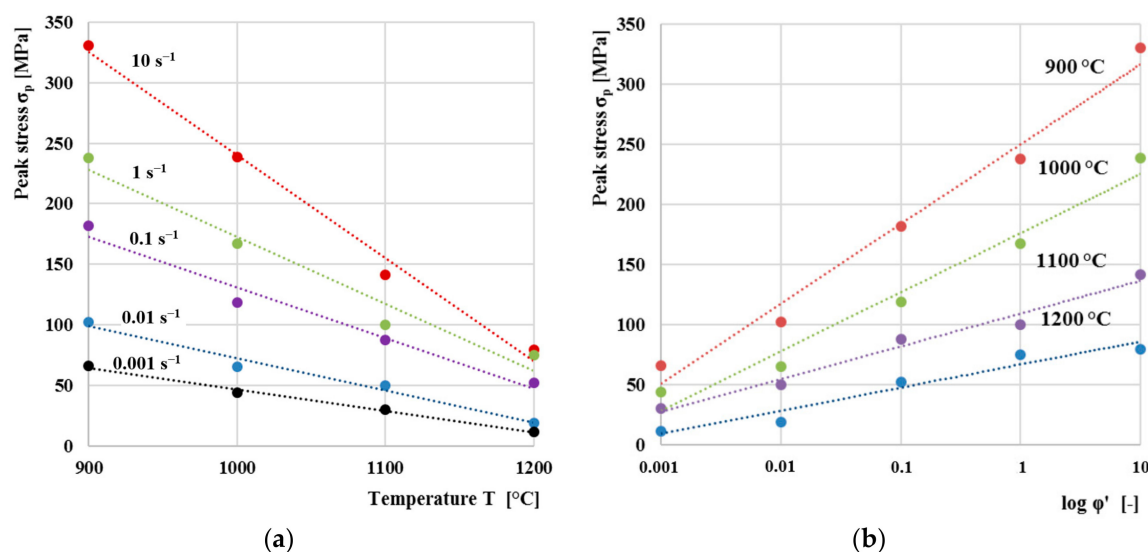


**Figure 14.** (a) dependence of strain resistance on temperature for individual strain rates; (b) dependence of strain resistance on strain rates for individual temperatures.

### 3.3. Microstructure Investigation

Microstructures of AISI 4340 for all deformation temperatures and two limiting values of deformation rates are in Figure 15 ( $\varphi' = 10 \text{ s}^{-1}$ ) and Figure 16 ( $\varphi' = 0.001 \text{ s}^{-1}$ ). The deformation temperature has a significant influence on the grain size [46]. In both shown cases of strain rates, grain size increases in proportion to temperature. This effect is more noticeable as the deformation rate decreases.

Microstructures of all deformation rates and two limiting values of temperatures are in Figure 17 ( $T = 900 \text{ }^{\circ}\text{C}$ ) and Figure 18 ( $T = 1200 \text{ }^{\circ}\text{C}$ ). The deformation rate has a lower effect on grain size than temperature. This effect can be observed in (Figure 16a–c) where the individual samples differ only minimally due to the changing deformation rate.

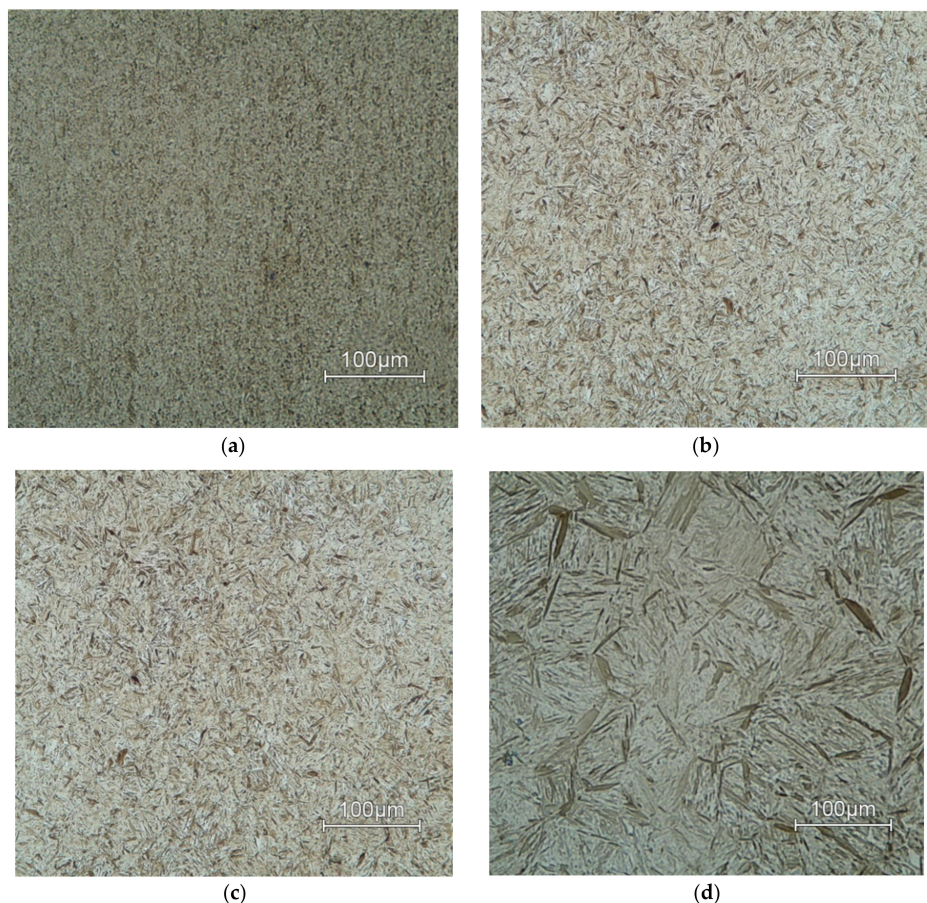


**Figure 15.** Microstructure of samples deformed at strain rate  $\varphi' = 10 \text{ s}^{-1}$  at temperature: (a)  $T = 900^\circ\text{C}$ ; (b)  $T = 1000^\circ\text{C}$ ; (c)  $T = 1100^\circ\text{C}$ ; (d)  $T = 1200^\circ\text{C}$ .

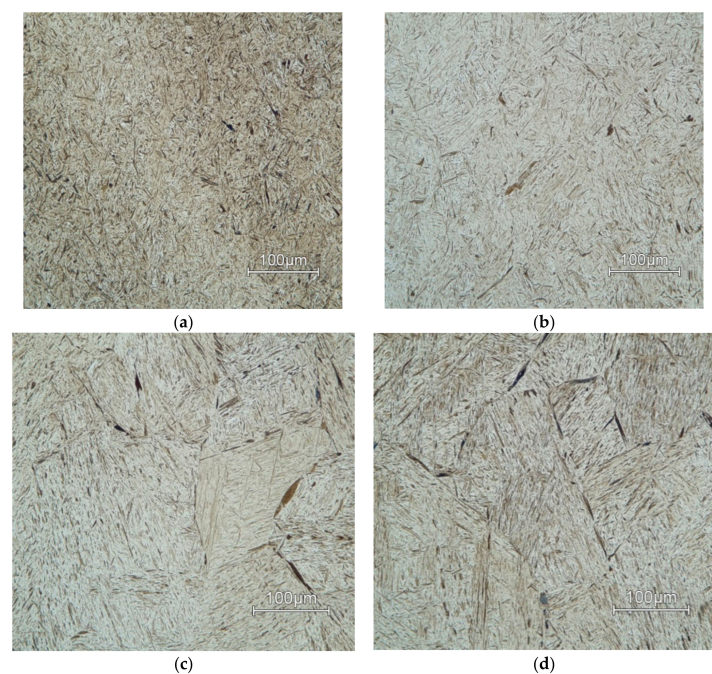


**Figure 16.** Microstructure of samples deformed at strain rate  $\varphi' = 0.001 \text{ s}^{-1}$  at temperature of: (a)  $T = 900^\circ\text{C}$ ; (b)  $T = 1000^\circ\text{C}$ ; (c)  $T = 1100^\circ\text{C}$ ; (d)  $T = 1200^\circ\text{C}$ .

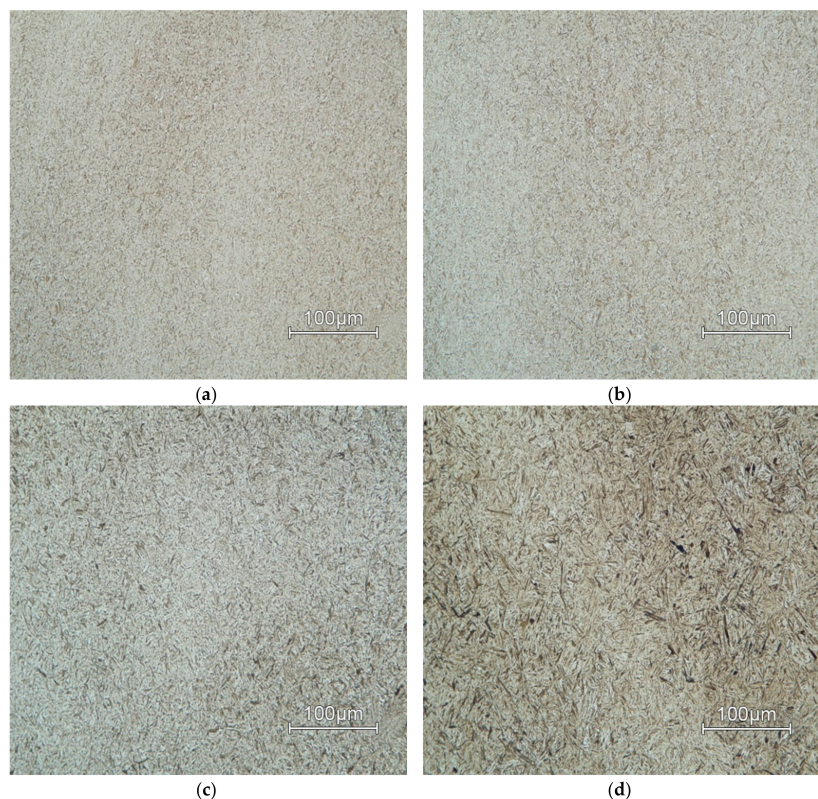


**Figure 17.** Microstructure of samples deformed at temperature of  $T = 900\text{ }^{\circ}\text{C}$  at strain rate: (a)  $1\text{ s}^{-1}$ ; (b)  $0.1\text{ s}^{-1}$ ; (c)  $0.01\text{ s}^{-1}$ ; (d)  $0.001\text{ s}^{-1}$ .

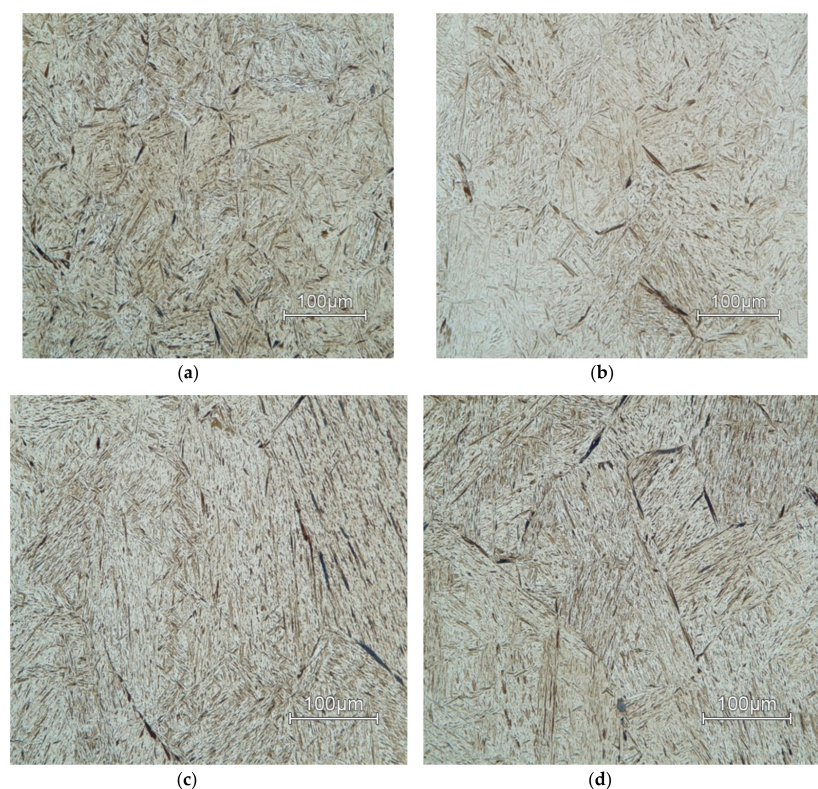


**Figure 18.** Microstructure of samples deformed at temperature of  $T = 1200\text{ }^{\circ}\text{C}$  at strain rate: (a)  $1\text{ s}^{-1}$ ; (b)  $0.1\text{ s}^{-1}$ ; (c)  $0.01\text{ s}^{-1}$ ; (d)  $0.001\text{ s}^{-1}$ .

The dynamic recrystallization occurs at higher temperatures, which suppresses the effect of deformation on the microstructure. Therefore, the microstructures are coarser at higher temperatures regardless of the deformation rate.

The combination of highest deformation rate  $\dot{\varphi} = 10 \text{ s}^{-1}$  and lowest temperature  $T = 900 \text{ }^{\circ}\text{C}$  has the most significant observed effect on grain size. At this temperature, there is no dynamic recrystallization present, and the grains remain deformed.

The correlations hardness versus logarithm of the strain rate (Figure 19a) and hardness versus deformation temperature (Figure 19b) indicate to be linear. As can be seen, the hardness increases linearly as the logarithm of strain rate rises. Diagram of final hardness versus peak stress  $\sigma_p$  (Figure 20) showed linear correlation between those variables.

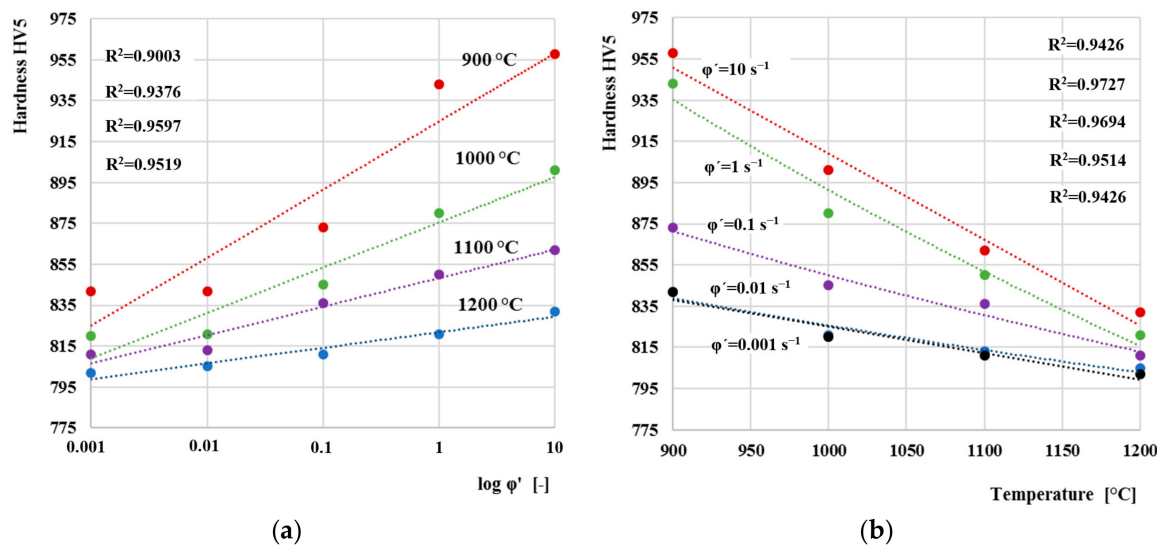


**Figure 19.** Influence of strain rate (a) and deformation temperature (b) on Vickers hardness (HV5) of AISI 4340 steel.

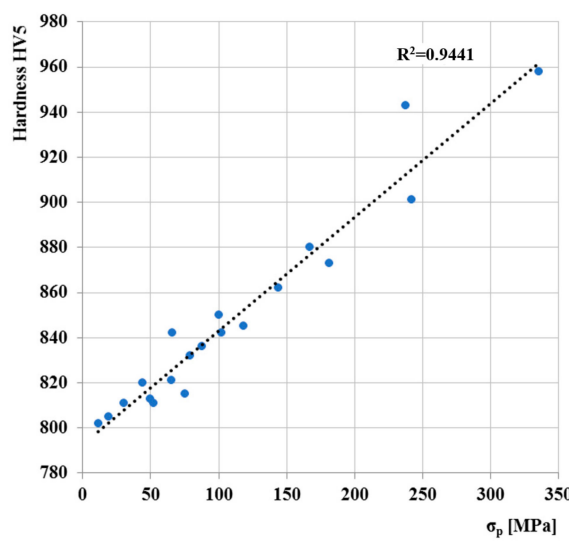


**Figure 20.** Total dependence of peak stress  $\sigma_p$  on the Vickers hardness.

#### 4. Conclusions

The behavior of AISI 4340 steel under various temperature and deformation conditions was investigated in this paper. Dilatometry analysis was designed to construct the CCT diagram of a high-strength steel from eight dilatation curves. The cooling rate was set from  $100 \text{ }^{\circ}\text{C/s}$  to  $0.01 \text{ }^{\circ}\text{C/s}$ .

Further analysis examined hot deformation behavior at various deformation temperatures from 900 °C to 1200 °C and strain rates from 0.001 s<sup>-1</sup> to 10 s<sup>-1</sup>. The following conclusions can be drawn from the present work:

1. Transformation temperatures have values of  $Ac_1 = 725$  °C to  $Ac_3 = 763$  °C. The selected austenitizing temperature thus guarantees full austenitizing throughout whole material bulk since it was set at 850 °C and holding time at this temperature was 30 min.
2. Average martensitic transformation start temperature is  $Ms = 282$  °C. The temperature is calculated from five dilatation curves (100, 10, 5, 1 and 0.5 °C/s) with martensitic transformation presence only. The  $Ms$  temperature softly decreases with reduction of cooling rate.
3. The highest Vickers hardness value of 850 was reached at the highest cooling rate of 100 °C/s and, conversely, at the lowest cooling rate of 0.01 °C/s the Vickers hardness of approximately half was reached, namely 423. The hardness decreases with decreasing of cooling rate, and this result is associated with the formation of individual structures.
4. Deformation rate has also significant effect on peak stress, which increases exponentially with increase in deformation rate. The highest value of peak stress ( $\sigma_p = 328$  MPa) was measured with a combination of the highest strain rate ( $\varphi' = 10$  s<sup>-1</sup>) and the lowest temperature ( $T = 900$  °C). The Arrhenius-type constitutive model can be used for prediction flow stress values of this type of steel with high prediction accuracy.
5. Microstructure investigations show that dynamic recrystallization takes a place at higher temperature (1200 °C), and grain coarsening occurs regardless of strain rate. Furthermore, high strain rate causes grain refinement. This effect is most noticeable at lower temperatures (900 °C) where the recrystallization is not present, and grains remain deformed with the result of very fine grains even after transformation of austenite to martensite or other phases.
6. The most noticeable effect on microstructure was observed with combination of the highest strain rate  $\varphi' = 10$  and the lowest temperature  $T = 900$  °C. This combination of deformation rate and temperature shows the most grain-refined microstructure.
7. The basic conclusion of the deformation analysis is that the peak stress decreases linearly with increasing deformation temperature and increases linearly with the deformation rate. The peak stress  $\sigma_p$  is very closely related to Vickers hardness where their dependence is linear.

**Author Contributions:** Conceptualization, M.K. and M.E.; methodology, M.K.; software, M.E.; validation, M.E., I.B. and J.M.; formal analysis, I.B. and M.B.; investigation, I.B.; resources, M.E.; data curation, M.K. and A.D.; writing—original draft preparation, I.B.; writing—review and editing, M.B. and J.M.; visualization, M.E.; supervision, M.K.; project administration, M.K. and A.D.; funding acquisition, I.B. All authors have read and agreed to the published version of the manuscript.

**Funding:** This research received no external funding.

**Acknowledgments:** This work was supported by the Slovak Research and Development Agency under the contract No. APVV-15-0710. This work was supported by the Science Grant Agency-project 1/0346/19. This work was also supported by the Research Agency of the Ministry of Education, Science, Research and Sport of the Slovak Republic under the contract (ITMS2014+) no. 313011W442-CEDITEK II.

**Conflicts of Interest:** The authors declare no conflict of interest.

## References

1. De Andrés, C.G.; Caballero, F.G.; Capdevila, C.; Álvarez, L.F. Application of dilatometric analysis to the study of solid–solid phase transformations in steels. *Mater. Charact.* **2002**, *48*, 101–111. [[CrossRef](#)]
2. Heidary, O.; Mirzaee, O.; Honarbakhsh Raouf, A.; Borhani, E. Texture development during austempering process of an AISI 4130 steel. *Mater. Sci. Eng. A* **2020**, *793*, 139751. [[CrossRef](#)]
3. Park, B.J.; Choi, J.M.; Lee, K.J. Analysis of phase transformations during continuous cooling by the first derivative of dilatation in low carbon steels. *Mater. Charact.* **2012**, *64*, 8–14. [[CrossRef](#)]
4. Bansal, G.; Srivastava, V.; Chowdhury, S.G. Role of solute Nb in altering phase transformations during continuous cooling of a low-carbon steel. *Mater. Sci. Eng. A* **2019**, *767*, 138416. [[CrossRef](#)]

5. Pashangeh, S.; Somani, M.; Banadkouki, S.S.G. Microstructural evolution in a high-silicon medium carbon steel following quenching and isothermal holding above and below the Ms temperature. *J. Mater. Res. Technol.* **2020**, *9*, 3438–3446. [[CrossRef](#)]
6. Chamanfar, A.; Chentouf, S.M.; Jahazi, M.; Lapierre-Boire, L.-P. Austenite grain growth and hot deformation behavior in a medium carbon low alloy steel. *J. Mater. Res. Technol.* **2020**, *9*, 12102–12114. [[CrossRef](#)]
7. Nawrocki, J.G.; Dupont, J.N.; Robino, C.V.; Puskar, J.D.; Marder, A.R. The mechanism of stress-relief cracking in a ferritic alloy steel. *Weld. J.* **2003**, *25*–35.
8. Yamashita, M.; Viswanathan, U.K.; Yamamoto, I.; Kobayashi, T. Service-induced changes in the microstructure and mechanical properties of a Cr-Mo-Ni-V turbine steel. *ISIJ Int.* **1997**, *37*, 1133–1138. [[CrossRef](#)]
9. Zhang, J.; Baker, T.N. Effect of equalization time on the austenite grain size of simulated thin slab direct charged (TSDC) vanadium microalloyed steels. *ISIJ Int.* **2003**, *43*, 2015–2022. [[CrossRef](#)]
10. Zhan, Y.Z.; Du, Y.; Zhuang, Y.H. Chapter Four—Determination of Phase Diagrams Using Equilibrated Alloys. In *Methods for Phase Diagram Determination*; Elsevier: Amsterdam, The Netherlands, 2007; pp. 108–150.
11. Lin, J.; Bailint, D.; Pietrzyk, M. *Microstructure Evolution in Metal Forming Processes*; Woodhead Publishing Limited: Cambridge, UK, 2012; p. 416.
12. Reza, T.; Abbas, N.; Reza, S. Drawing of CCCT diagrams by static deformation and consideration deformation effect on martensite and bainite transformation in NiCrMoV steel. *J. Mater. Process. Technol.* **2008**, *196*, 321–331. [[CrossRef](#)]
13. Tamura, I.; Sekine, H.; Tanaka, T.; Ouchi, C. *Thermomechanical Processing of High Strength Low Alloy Steels*; Butterworth-Heinemann: Oxford, UK, 1998; p. 256.
14. Back, J.G.; Surreddi, K.B. Microstructure analysis of martensitic low alloy carbon steel samples subjected to deformation dilatometry. *Mater. Charact.* **2019**, *157*, 109926. [[CrossRef](#)]
15. García-Mateo, C.; Caballero, F.G.; Capdevila, C.; De Andrés, C.G. Estimation of dislocation density in bainitic microstructures using high-resolution dilatometry. *Scr. Mater.* **2009**, *61*, 855–858. [[CrossRef](#)]
16. Yang, J.; Cao, B.; Wu, Y.; Gao, Z.; Hu, R. Continuous cooling transformation (CCT) behavior of a high Nb-containing TiAl alloy. *Materialia* **2019**, *5*, 100169. [[CrossRef](#)]
17. Pickering, E.J.; Collins, J.; Stark, A.; Connor, L.D.; Kiely, A.A.; Stone, H.J. In situ observations of continuous cooling transformations in low alloy steels. *Mater. Charact.* **2020**, *165*, 110355. [[CrossRef](#)]
18. Barényi, I.; Majerík, J.; Bezceny, J.; Krba, M.; Sedláček, J.; Jaroš, A. Material and technological aspects while processing of selected ultrahigh strength steel. *Manuf. Technol.* **2019**, *19*, 184–189.
19. Hunkel, M.; Surm, H.; Steinbacher, M. *Handbook of Thermal Analysis and Calorimetry*; Elsevier: Amsterdam, The Netherlands, 2018; p. 860.
20. Berkowski, L. The influence of warm plastic deformation on the structure and on the applicable properties of high speed steel. *J. Mater. Process. Technol.* **1996**, *60*, 637–641. [[CrossRef](#)]
21. Krishnan, R.S.; Srinivasan, R.; Devanarayanan, S.; Pamplin, B.R. *Thermal Expansion of Crystals*; Pergamon Press: Oxford, UK, 1979; p. 316.
22. Stahl-Eisen-Prüfblatt. *Aufstellung von Zeit-Temperatur-Umwandlungsschaubildern für Eisenlegierungen*; STAHL-EISEN-Prüfblätter des Vereins Deutscher Eisenhüttenleute, Matplus GmbH: Wuppertal, Germany, 1990.
23. Stahl-Eisen-Prüfblatt. *Guidelines for Preparation, Execution and Evaluation of Dilatometric Transformation Test on Iron Alloys*; STAHL-EISEN-Prüfblätter des Vereins Deutscher Eisenhüttenleute, Willey: Hoboken, NJ, USA, 1998.
24. ASTM Committee A01 on Steel, Stainless Steel and Related Alloys. *Standard Practice for Quantitative Measurement and Reporting of Hypoeutectoid Carbon and Low-Alloy Steel Phase Transformations*; ASTM International: West Conshohocken, PA, USA, 2004.
25. Krizan, D.; Spiradek-Hahn, K.; Pichler, A. Relationship between microstructure and mechanical properties in Nb-V microalloyed TRIP steel. *Mater. Sci. Technol.* **2014**, *31*, 661–668. [[CrossRef](#)]
26. Spigarelli, S.; Cabibbo, M.; Evangelista, E.; Bidulská, J. A study of the hot formability of an Al-Cu-Mg-Zr alloy. *J. Mater. Sci.* **2003**, *38*, 81–88. [[CrossRef](#)]
27. Ebrahimi, R.; Najafizadeh, A. A new method for evaluation of friction in bulk metal forming. *J. Mater. Process. Technol.* **2004**, *152*, 136–143. [[CrossRef](#)]
28. Zener, C.; Hollomon, J.H. Effect of Strain Rate Upon Plastic Flow of Steel. *J. Appl. Phys.* **1944**, *15*, 22–32. [[CrossRef](#)]

29. Wang, Y.; Li, J.; Xin, Y.; Li, C.; Cheng, Y.; Chen, X.; Rashad, M.; Liu, B.; Liu, Y. Effect of Zener–Hollomon parameter on hot deformation behavior of CoCrFeMnNiCo<sub>0.5</sub> high entropy alloy. *Mater. Sci. Eng. A* **2019**, *768*, 138483. [[CrossRef](#)]
30. Shang, X.; Cui, Z.; Fu, M.W. A ductile fracture model considering stress state and Zener–Hollomon parameter for hot deformation of metallic materials. *Int. J. Mech. Sci.* **2018**, *144*, 800–812. [[CrossRef](#)]
31. Krbata, M.; Eckert, M.; Krizan, D.; Barenyi, I.; Mikušová, I. Hot Deformation Process Analysis and Modelling of X153CrMoV12 Steel. *Metals* **2019**, *9*, 1125. [[CrossRef](#)]
32. Bräutigam–Matus, K.; Altamirano-Guerrero, G.; Salinas-Rodríguez, A.; Valdés, A.F.; Goodwin, F. Experimental Determination of Continuous Cooling Transformation (CCT) Diagrams for Dual-Phase Steels from the Intercritical Temperature Range. *Metals* **2018**, *8*, 674. [[CrossRef](#)]
33. Trzaska, J.; Dobrzański, L.A. Modelling of CCT diagrams for engineering and constructional steels. *J. Mater. Process. Technol.* **2007**, *192*, 504–510. [[CrossRef](#)]
34. Zhang, X.; Wang, H.; Hickel, T.; Rogal, J.; Li, Y.; Neugebauer, J. Mechanism of collective interstitial ordering in Fe–C alloys. *Nat. Mater.* **2020**, *19*, 849–854. [[CrossRef](#)]
35. Pan, L.; Kwok, C.T.; Lo, K.H. Effect of Multiple-Pass Friction Stir Processing on Hardness and Corrosion Resistance of Martensitic Stainless Steel. *Coatings* **2019**, *9*, 620. [[CrossRef](#)]
36. Krbata, M.; Majerík, J.; Barényi, I.; Eckert, M. Experimental determination of continuous cooling transformation diagram for high strength steel OCHN3MFA. *IOP Conf. Ser. Mater. Sci. Eng.* **2020**, *776*. [[CrossRef](#)]
37. Barenyi, I.; Krbaťa, M.; Majerík, J. Structure Evolution of 33NiCrMo15 Steel in Relation to Tempering Temperature. In Proceedings of the 30th International DAAAM Symposium “Intelligent Manufacturing & Automation”, Zadar, Croatia, 23–26 October 2019; 30, pp. 800–805.
38. Boyer, H.; Gray, A.G. *Atlas of Isothermal Transformation and Cooling Transformation Diagrams*; American Society for Metals: Cleveland, OH, USA, 1977; p. 181.
39. Samadi Shahreza, Z.; Dini, G.; Taherizadeh, A. Improving the Microstructure, Mechanical and Magnetic Properties of AISI 4340 Steel Using the Heat Treatment Process. *Int. J. ISSI* **2013**, *10*, 18–22.
40. Penha, R.N.; Vatavuk, J.; Couto, A.A.; de Lima Pereira, S.A.; De Sousa, S.A.; de, C.F. Canale, L. Effect of chemical banding on the local hardenability in AISI 4340 steel bar. *Eng. Fail. Anal.* **2015**, *53*, 59–68. [[CrossRef](#)]
41. Nasar, A.A. Thermomechanical Processing of 34CrNiMo6 Steel for Large Scale Forging. Ph.D. Thesis, University of Sheffield, Sheffield, UK, 2014; p. 276.
42. Popescu, N.; Cojocaru, M.; Mikhailov, V. Experimental studies on bulk tempering of 34CrNiMo6 steel. *Surf. Eng. Appl. Electrochem.* **2012**, *48*, 28–34. [[CrossRef](#)]
43. Sajadifar, S.V.; Yapıcı, G.G.; Ketabchi, M.; Bemanizadeh, B. High Temperature Deformation Behavior of 4340 Steel: Activation Energy Calculation and Modeling of Flow Response. *J. Iron Steel Res. Int.* **2013**, *20*, 133–139. [[CrossRef](#)]
44. Silva, K.; Brito, P.; Santos, I.; Câmara, M.; Abrão, A. The behaviour of AISI 4340 steel coatings on low carbon steel substrate produced by friction surfacing. *Surf. Coatings Technol.* **2020**, *399*, 126170. [[CrossRef](#)]
45. Medina, S.F.; Hernandez, C. General expression of the Zener–Hollomon parameter as a function of the chemical composition of low alloy and microalloyed steels. *Acta Mater.* **1996**, *44*, 137–148. [[CrossRef](#)]
46. Barényi, I.; Krbaťa, M.; Majerík, J.; Mikušová, I. Effect of deformation parameters on microstructure evolution and properties of 33NiCrMo15 steel. *IOP Conf. Ser. Mater. Sci. Eng.* **2020**, *776*. [[CrossRef](#)]

**Publisher’s Note:** MDPI stays neutral with regard to jurisdictional claims in published maps and institutional affiliations.



© 2020 by the authors. Licensee MDPI, Basel, Switzerland. This article is an open access article distributed under the terms and conditions of the Creative Commons Attribution (CC BY) license (<http://creativecommons.org/licenses/by/4.0/>).